Nanotechnology **19** (2008) 315301 (8pp) doi:10.1088/0957-4484/19/31/315301

Non-planar nanofluidic devices for single molecule analysis fabricated using nanoglassblowing

Elizabeth A Strychalski[1], Samuel M Stavis[2] and Harold G Craighead[3]

[1] Department of Physics, Cornell University, Ithaca, NY 14853, USA
[2] Semiconductor Electronics Division, National Institute of Standards and Technology, Gaithersburg, MD 20899, USA
[3] School of Applied and Engineering Physics, Cornell University, Ithaca, NY 14853, USA

E-mail: eas58@cornell.edu, sstavis@nist.gov and hgc1@cornell.edu

Received 15 April 2008, in final form 23 May 2008
Published 17 June 2008
Online at stacks.iop.org/Nano/19/315301

Abstract

A method termed 'nanoglassblowing' is presented for fabricating integrated microfluidic and nanofluidic devices with gradual depth changes and wide, shallow nanochannels. This method was used to construct fused silica channels with out-of-plane curvature of channel covers from over ten micrometers to a few nanometers, nanochannel aspect ratios smaller than 2×10^{-5}:1 (depth:width), and nanochannel depths as shallow as 7 nm. These low aspect ratios and shallow channel depths would be difficult to form otherwise without collapse of the channel cover, and the gradual changes in channel depth eliminate abrupt free energy barriers at the transition from microfluidic to nanofluidic regions. Devices were characterized with atomic force microscopy (AFM), white light interferometry, scanned height measurements, fluorescence intensity traces, and single molecule analysis of double-stranded deoxyribonucleic acid (DNA) velocity and conformation. Nanochannel depths and aspect ratios formed by nanoglassblowing allowed measurements of the radius of gyration, R_g, of single λ DNA molecules confined to slit-like nanochannels with depths, d, ranging from 11 nm to 507 nm. Measurements of R_g as a function of d agreed qualitatively with the scaling law $R_g \propto d^{-0.25}$ predicted by Brochard for nanochannel depths from 36 nm to 156 nm, while measurements of R_g in 11 nm and 507 nm deep nanochannels deviated from this prediction.

1. Introduction

Nanofluidic devices are used for a variety of research applications, including biomolecular analysis [1–6], and interest in slit-like nanochannels in particular continues to grow [7–16]. The utility of these structures remains limited, however, by planar device architectures as well as the need for high resolution nanofabrication processes [17, 18]. A simple fabrication method termed 'nanoglassblowing' is presented here that enables control over out-of-plane curvature of channel surfaces and improves attainable aspect ratios of shallow nanochannels in device regions without curvature. This method is based on continuous nanoscale channel depth variation, which arises due to the outward deflection of a softened glass channel cover by increased air pressure during annealing of a bonded device. While the plastic deformation of silicon and borosilicate glass at the micrometer scale has been demonstrated [19, 20], such fabrication techniques have not been characterized previously at the nanometer length scale or exploited to construct fluidic systems. Nanoglassblowing was used here to fabricate integrated microfluidic and nanofluidic devices from fused silica with out-of-plane channel curvature from over ten micrometers to a few nanometers, nanochannel depths as shallow as 7 nm, and nanochannel aspect ratios smaller than 2×10^{-5}:1 (depth:width).

Because this method enables device bonding without the collapse of low aspect ratio, slit-like nanochannels, contact photolithography can be used to pattern wide precursor trenches. This facilitates the fabrication of nanochannels that are both shallow and wide, a combination needed to prevent

 © 2008 IOP Publishing Ltd Printed in the UK

hydrodynamic or other nanochannel edge interactions [1, 10] that could hinder dynamic physical measurements, such as the observation of long DNA molecules in constrained environments or continuous flow molecular analysis. The ability to subsequently fabricate variable nanochannel depths from this single layer of photolithography and etch depth obviates the need for multiple levels of aligned lithography. These fabrication benefits permit the seamless integration of device features across the centimeter to nanometer length scales relevant to miniaturized fluidic systems, including the critical micrometer-to-nanometer transition. When combined with the desirable optical and chemical properties of fused silica, the resulting devices are well suited to the manipulation and observation of single biomolecules [3], as demonstrated here.

The presence of access holes during annealing, the channel width, the channel etch depth, and the device geometry were each observed to reproducibly affect the amount of out-of-plane curvature that occurred, establishing several means to influence final device geometry. These results were used to design and fabricate non-planar t-junction and h-junction nanofluidic devices for single molecule manipulation and analysis. These architectures demonstrate the integration of non-planar channel surfaces arising from nanoglassblowing into standard microfluidic and nanofluidic formats. For the purposes of this work, the essential features of both device geometries are similar: channels with micrometer or submicrometer depths and out-of-plane surface curvature to serve as intermediate loading regions between macroscopic device reservoirs and nanochannels, planar slit-like nanochannels for molecular confinement and analysis, and non-planar interfaces smoothly connecting the deep loading regions to the shallow nanochannels.

The t-junction device was utilized to demonstrate the advantageous entropic and electrokinetic properties of a continuous, non-planar microfluidic-to-nanofluidic interface. While an abrupt change in device depth is necessary for some applications, such as entropic trapping [21–23], a more gradual depth change is needed for others, such as the steady loading of DNA into regions of high confinement. This is particularly important, for example, for the continuous flow analysis of mixtures of DNA molecules of various lengths using nanofluidic channels [23, 24]. Accordingly, rather than subject DNA molecules to a sudden increase in length-dependent entropic confinement due to an abrupt reduction of channel depth, the gradual depth change in devices fabricated using nanoglassblowing decreases the entropic barrier encountered by DNA molecules entering the nanochannel [17], facilitating uniform entry and reducing clogging. Electro-osmotic backflow at the nanochannel entrance, previously observed to be detrimental in fused silica nanofluidic devices with abrupt depth changes [12], was not seen in devices constructed using nanoglassblowing, removing the need for chemical modification of channel surfaces. This smooth depth transition was probed using single molecule measurements of DNA velocity and exploited to aid in the loading and extension of DNA molecules into slit-like nanochannels as shallow as 7 nm.

H-junction devices were then used for single molecule measurements of the radius of gyration of λ DNA in slit-like nanochannels of varying depth. These nanochannels were shallower and wider than those used in previous studies of single DNA molecule dynamics, which were limited to depths of 75 nm or above and widths up to 150 μm [7–9, 15, 16]. The resulting radius of gyration measurements provide increased insight into the behavior of DNA strongly confined by channel height, but unconfined by channel width, for which a theoretical description is lacking [7, 25]. Such an understanding could be useful for the further development of miniaturized biomolecular separations, single molecule sequencing, and other technologies for nanofluidic biomolecular analysis.

In addition to the applications demonstrated here, nanoglassblowing has further potential for the fabrication of other micro- and nanostructures for applications that would benefit from gradual contours or very shallow channels, such as nanofluidic devices for the separation of biomolecules, nanoparticles, and cells [26, 27] and optofluidic lenses and waveguides [28, 29]. Microfluidic devices for cellular manipulation and analysis may also benefit from smoother fluid flow due to gradual channel depth transitions, as well as the ability to variably confine individual cells and culture continuous cell layers across regions of changing device depth [30–32].

2. Fabrication

To make devices using nanoglassblowing, 100 mm diameter, 500 μm thick fused silica channel substrate wafers (7980 fused silica, Corning Inc., Canton, NY; Mark Optics, Santa Ana, CA) were coated with photoresist, patterned using a contact aligner, and wet etched at 22 °C without agitation using 100:1 buffered oxide etch with surfactant (Ultra Etch, Air Products and Chemicals Inc., Allentown, PA). If access holes were desired prior to annealing, additional resist was spun onto the wafer, and access holes were defined using micro-abrasive blasting. The wafers were then cleaned using a series of soapy water and solvent rinses and 2–4 h of light agitation in isopropyl alcohol. AFM images (Digital Instruments Dimension 3000, Veeco Instruments, Inc., Santa Barbara, CA), giving depth and surface roughness information for all devices prior to bonding, were obtained in tapping mode with probes (TESP, Veeco Instruments, Inc.) specified to have a tip radius $<$10 nm, and were analyzed using DI Nanoscope software (Digital Instruments/Veeco). Roughness data are given as root-mean-square values and were calculated from 25 μm^2 image areas. Following characterization of the etched surfaces, bonding of the channel substrate wafers to 100 mm diameter, 170 μm thick fused silica cover wafers was accomplished via additional cleaning steps. The 500 μm thick wafers were treated with a hot piranha solution (3:1 mixture of sulfuric acid and hydrogen peroxide). All wafers were subsequently rinsed in deionized water, dried, and exposed to oxygen plasma at 950 W for 10 min. Immediately thereafter, the channel substrate and cover were touched together, and trapped air was massaged out by hand. Nanoglassblowing

occurred while bonded devices were annealed at atmosphere using the following process: ramp from room temperature at 150 °C h^{-1} to 1050 °C, dwell 6 h at 1050 °C, and cool to room temperature. For the creation of access holes after bonding and annealing, micro-abrasive blasting was used, followed by water and solvent rinses, sonication in isopropyl alcohol, and sealing using 170 μm thick fused silica wafer pieces and silicone sealant.

3. Results and discussion

The out-of-plane curvature of devices fabricated using nanoglassblowing was measured via several techniques. White light interference patterns in air-filled devices provided a convenient means for estimating the amount of curvature of internal channel surfaces for depths below approximately 2 μm [33, 34]. Infusion with fluorescent dye solution revealed channels a few tens of nanometers and below in depth. Scanned height measurements across covers over channels indicated the amount of external out-of-plane deflection of the channel cover (Tencor P-10 Surface Profiler). The conformation of individual DNA molecules was also used to probe internal channel geometries. Out-of-plane curvature of the 500 μm thick channel substrates was not observed.

The presence or absence of channel access holes during annealing was observed to influence the out-of-plane curvature due to nanoglassblowing in channels of differing width but identical etch depth. The deformation of a softened cover over a nanochannel without access holes can be likened to heated air expanding molten glass at the end of a closed blowpipe during traditional glassblowing. Access holes allow pressure equilibration between the air inside a channel and the annealing furnace atmosphere, in a process similar to a glassblower letting heated air escape from the blowpipe. Although traditional glassblowing makes use of molten glass, and nanoglassblowing as demonstrated here uses glass wafers heated only slightly above the annealing temperature of 1042 °C, both techniques rely on heated and expanding air to help shape glass with reduced viscosity due to increased temperature. In general, a channel without an access hole exhibited greater out-of-plane curvature than the same channel with an access hole (table 1). Some nanoglassblowing occurred even in channels with access holes, as protective silicon wafers were used during annealing, and air may not have escaped the devices freely through the access holes. Figure 1(a) shows side-view schematics of channels differing only in the presence or absence of an access hole during annealing. The etch depth was (32 ± 2) nm, while the maximum channel depth was attained by nanoglassblowing. All etch depths are quoted with errors of one standard deviation, which reflect variations in etch depth due to surface roughness and the etch process. One wafer of this etch depth was made with each set of corresponding channels patterned three times. Side-by-side patterning of corresponding channels reduced the likelihood that variations in stress release contributed significantly to differences in out-of-plane deflection. 500 μm and 170 μm thick wafers annealed prior to bonding, in order to release latent stress from the wafer manufacturing process, exhibited enough wafer

Table 1. Dependence of out-of-plane curvature on access holes and channel width for channels with (32 ± 2) nm etch depth.

	Maximum out-of-plane deflection of channel cover (nm)[a]	
Channel width (μm)	Access hole	No access hole
100	0	10
250	10	30
500	30	180
750	50	180
1000	70	510
1500	200	2 200
2500	200	11 000
5000	120	17 000
7500	3700	11 000

[a] Out-of-plane deflection values were obtained from individual scanned height measurements.

deformation to prevent device bonding but not to account completely for the amount of out-of-plane curvature observed. Top-down brightfield optical micrographs (figure 1(b)) show white light interference patterns due to channel depth variation from nanoglassblowing, and figure 1(c) shows individual representative scanned height measurements along the dotted lines in figures 1(a) and (b). Simple calculations using the ideal gas law agreed qualitatively with observations of out-of-plane deflection due to nanoglassblowing, and a more comprehensive model taking into account information regarding the glass's thermal and mechanical properties, more complete measurements of channel cover curvature, and measurements of air pressure inside channels after bonding is expected to provide more accurate predictions for the results of nanoglassblowing. More thorough discussion and modeling of similar systems is presented by Huff *et al* [20] and Eklund and Shkel [19].

The out-of-plane curvature due to nanoglassblowing for h-junction devices with slit-like nanochannels of the same length and width was also observed to depend upon etch depth (table 2). One wafer for each etch depth was patterned with four devices each. Channels etched more deeply held a greater volume of expanding air; consequently, the covers over these deeper channels tended to curve more than for shallower channels of the same width. As etch depth decreased, localized regions of out-of-plane curvature—bubbles—formed between regions of little or no curvature. Bubble formation may have been promoted by local stress release. For channel widths below approximately 200 μm, no out-of-plane curvature was observed using white light interferometry for all etch depths.

Nanoglassblowing also enabled the construction of planar slit-like nanochannels without observable out-of-plane deflection or collapse, with aspect ratios an order of magnitude smaller than similar channels reported using other fabrication techniques [35], and half the smallest aspect ratio reported for slit-like nanochannels [18]. It is hypothesized that increased air pressure in channels during annealing prevented collapse but was not sufficient for nanoglassblowing. This allowed successful fabrication of very shallow nanochannels with depths limited ultimately by the surface roughness of the channel substrate and cover, as seen when DNA molecules

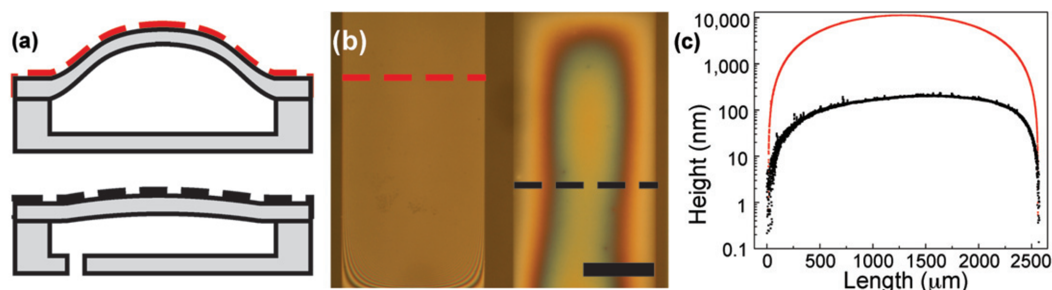

Figure 1. Effects of nanoglassblowing on channel geometry. (a) Illustrated side views of otherwise identical channels annealed without and with access holes demonstrate the effects of these holes on nanoglassblowing. The red and black dashed lines in (a) and (b) correspond to the locations of the red and black scanned height measurements in (c). (b) White light interference patterns are visible in this photograph of adjacent channels with (32 ± 2) nm etch depths (scale bar: 1.25 mm). The left channel has no access hole, while the right channel has an access hole through which air could pass during bonding and annealing. (c) Out-of-plane curvature varies smoothly across the channel widths, as seen in these single representative scans.

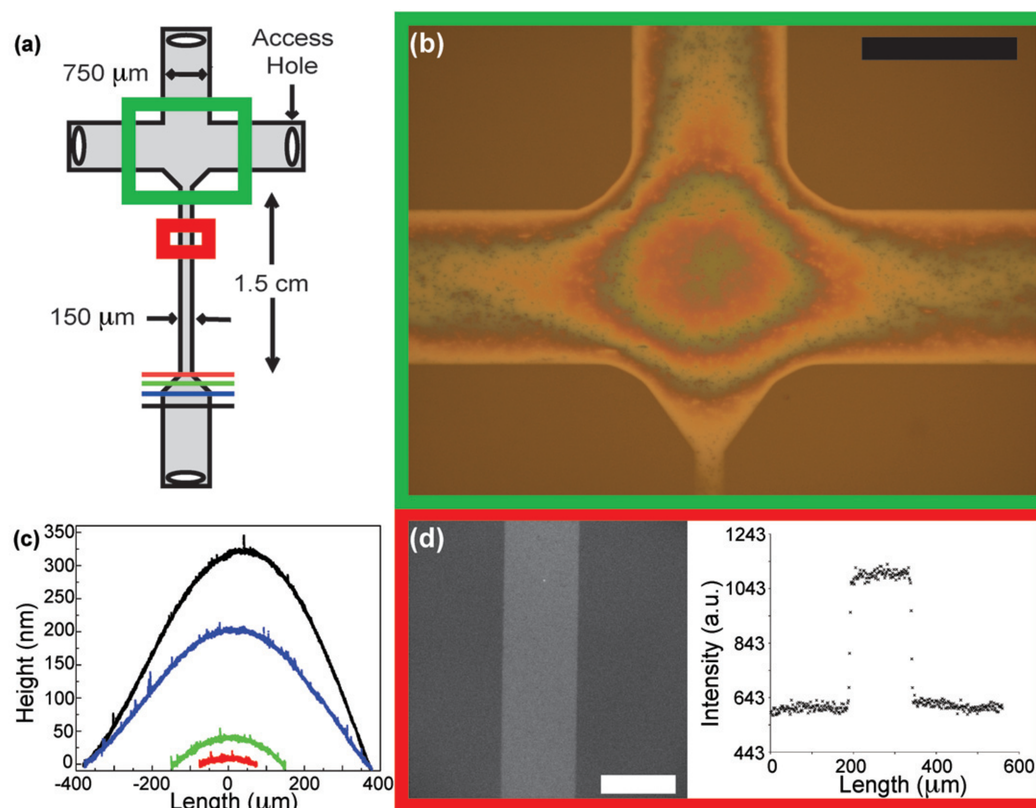

Figure 2. T-junction nanofluidic device with non-planar micro-to-nano interface and planar nanoslit. (a) Top-down schematic of the t-junction device, which had an etch depth of (10.5 ± 0.2) nm. The device geometry was chosen to give out-of-plane curvature in 750 μm wide loading channels and no curvature in the 150 μm wide channel. (b) A brightfield optical micrograph of the green boxed area in (a) shows white light interference patterns (scale bar: 750 μm). (c) Individual scanned height measurements across the tapered width region, color-coded to the colored lines in (a), indicate decreasing channel depth as channel width decreases. (d) A fluorescence micrograph of the red boxed area in (a) and a fluorescence intensity trace across the image imply no collapse or out-of-plane curvature (scale bar: 150 μm).

were driven into the 7 nm deep channels in table 2 (data shown below). For comparison, 150 μm wide, 8 nm deep slit-like nanochannels fabricated without nanoglassblowing collapsed consistently ($n = 14$), while the same device geometry with 25 nm deep slit-like nanochannels did not collapse ($n = 14$).

In order to establish the ability to incorporate both out-of-plane curvature and extremely shallow channels into a functional nanofluidic device, the t-junction device shown in figure 2 was created. 750 μm wide loading and exit regions were patterned on either side of a 150 μm wide channel, with a gradually tapered width in between (figure 2(a)). These widths were chosen to ensure sufficient out-of-plane curvature in loading and exit regions to aid in the introduction of DNA into the device and preclude out-of-plane curvature in the 150 μm wide channel. The etch depth was (10.5 ± 0.2) nm, with five devices patterned on the wafer. Figure 2(b) shows

Table 2. Dependence of out-of-plane curvature on channel width and etch depth for slit-like nanochannels in h-junction devices annealed with access holes.

	Etch depth (nm)[a]				
	155.5 ± 2.2	69.6 ± 1.4	35.6 ± 1.0	11.3 ± 0.6	7.1 ± 2.1
Channel width (μm)	Maximum channel depth (nm)[b]				
2					
5					
10					
25	Etch depth	Etch depth	Etch depth	Etch depth	Etch depth
75					
100					
200					
300					Localized curvature between regions without out-of-plane curvature, i.e. bubbles
400				Localized curvature between regions without out-of-plane curvature, i.e. bubbles	
500					
600					
700					
800	180				
900		180			
1000	200				
1500	280	200			
2000	460	530			

[a] Channel etch depths were measured via atomic force microscopy. Errors are one standard deviation.

[b] Maximum channel depth was determined using white light interferometry [28].

a brightfield optical micrograph of the air-filled device after annealing without access holes. White light interferometry confirmed the out-of-plane curvature of the 750 μm wide channels and indicated a maximum depth of approximately 880 nm [32]. Darker features within the channels were attributed to surface roughness, which is 0.3 nm. The bond separated slightly at the intersection of the loading channels, visible as rounded corners. White light interference patterns show gradual depth reduction in the tapered width region that was verified by individual scanned height measurements at four locations (figure 2(c)). Scan locations in figure 2(c) are color-coded to the colored lines in figure 2(a). The small out-of-plane deflection relative to the cover thickness and channel widths allows the assumption that these measurements approximate the internal channel surface curvature. Fluid reservoirs were affixed to access holes using silicone sealant, and devices were filled via capillary action with a solution of 70% ethanol and 30% 18 MΩ water. This was replaced with 5X tris-borate-EDTA buffer (TBE) with 2% beta-mercaptoethanol (v/v) (both chemicals Sigma Aldrich, St Louis, MO) to prevent photobleaching of fluorescent dye and photocleaving of DNA molecules. Nanoglassblowing did not occur in the 150 μm wide channel, as evidenced by an intensity trace across this channel while filled with rhodamine B (Sigma) fluorescent dye solution (figure 2(d)). Rhodamine B was prepared at 100 μM in 18 MΩ water, diluted to 14.3 μM during use, and driven through channels electrokinetically.

Fluorescence was visualized using an inverted microscope (IX70 Olympus America, Melville, NY), 40 × 1.15 NA water immersion or 60× 0.9 NA air objectives (Olympus), and filter cube sets XF100-2 (Omega Optical Inc., Brattleboro, VT) and TXRED-4040B-OMF-ZERO (Semrock, Rochester, NY). Devices were illuminated with a broad spectrum light source (Exfo X-Cite 120, Vanier, Quebec, Canada). Images were captured using a Cascade 512b (Photometrics, Tucson, AZ) and custom software written in Labview (National Instruments Corporation, Austin TX). Image processing was done using custom software written in Matlab (The MathWorks, Natick, MA). Dye and DNA were driven electrokinetically using voltage supplied by Stanford Research Systems PS325 (Sunnydale, CA) or Keithley 230 (Keithley Instruments, Inc., Cleveland, OH) DC power supplies through device reservoirs using gold electrodes.

The gradual change in channel depth between microchannels and nanochannels facilitated the loading and extension of λ DNA molecules into extremely shallow slit-like nanochannels, when compared to nanofluidic devices with abrupt depth changes [12]. This highlights an important aspect of nanoglassblowing, namely, the length along a channel over which curvature is observed. The depth change of the channel must be small across the length of a molecule in order to effectively reduce or eliminate the entropic barrier; loading very large biomolecules, such as genomic DNA, requires a correspondingly long region of gradual depth change between loading channels and nanochannels. While the non-planar channel features of previous studies [17, 18] occur over tens of micrometers and are akin to inclined planes, the t-junction device, for example, exhibits gradual depth change along the entire 420 μm long tapered width region. Various device geometries allowed adjustment of this distance along the channel over which gradual depth change occurred between loading channels and nanochannel entrances from tens of micrometers to millimeters (data not shown). Changes in bonding or annealing conditions may also influence this distance but were not

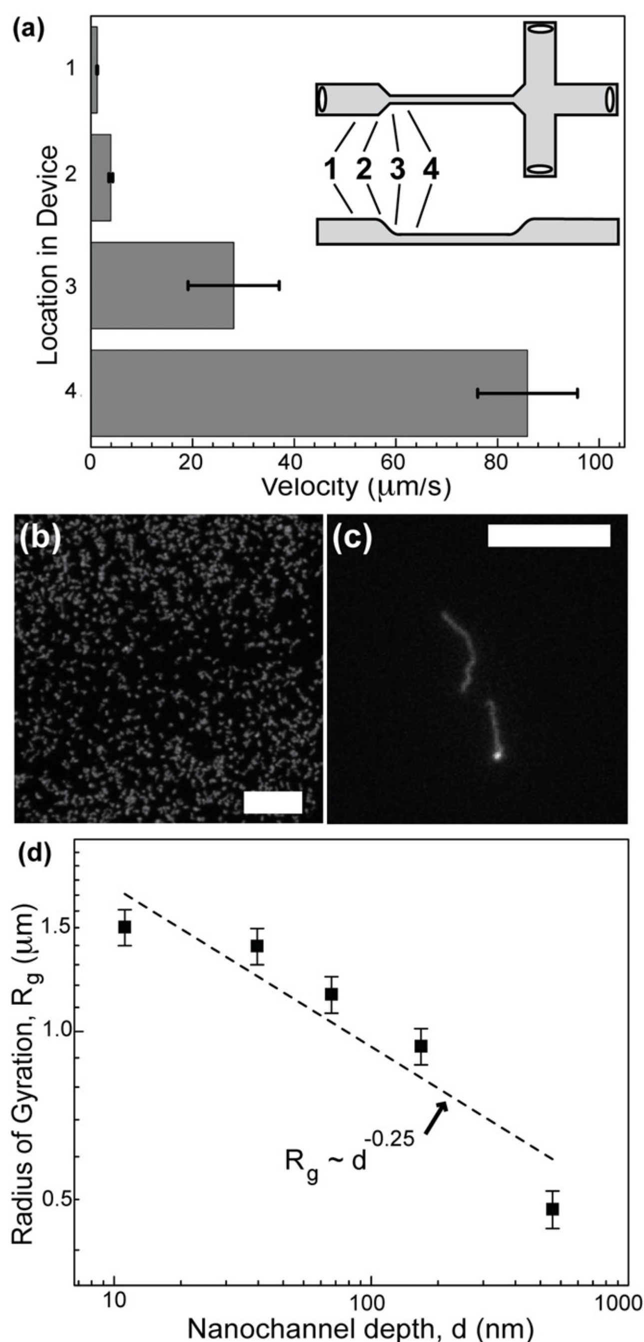

Figure 3. Single molecule analysis of DNA velocity and conformation. (a) Velocity of λ DNA molecules plotted for four locations in the t-junction device. The locations are indicated in top-down and side-view device schematics. Three molecules were analyzed for each location, and error bars are one standard deviation. (b) λ DNA molecules in their bulk conformation in a deep, curved loading region (scale bar: 10 μm). (c) λ DNA molecules electrophoresing through a 7 nm deep and 300 μm wide slit-like nanochannel (scale bar: 10 μm). (b) and (c) show unprocessed image data. (d) Radius of gyration, R_g, is plotted against nanochannel depth, d. Each data point combines the results from ten λ DNA molecules and is corrected for the effects of diffraction limited optical resolution and image pixelation. Error bars represent the addition of one standard deviation of the mean R_g and estimates of error from optical resolution, image pixelation, digital filtering, and noise thresholding. Uncertainty values for the nanochannel depths are smaller than the data symbols. Brochard's predicted theoretical scaling is shown as a dashed line overlaid on the experimental data. (b), (c), and (d) used h-junction devices.

investigated here. Because nanoglassblowing gives curvature across a channel width in addition to its length, more complex shapes can also be fabricated, such as domes (center of figure 2(b)).

This gradual channel depth decrease between 750 μm and 150 μm wide channels was probed using the observed velocity of single DNA molecules in this region of the t-junction device (figure 3(a)). λ DNA (New England Biolabs, Ipswich, MA) at a concentration of 12.5 μg ml^{-1} in 5X TBE was labeled with YOYO-1 (Invitrogen, Carlsbad, CA) at a 5:1 dye to base pair ratio and diluted by a factor of 50 before use. Videos were taken at 10 frames s^{-1} as individual DNA molecules moved from the 750 μm wide, curved loading region into the 150 μm wide channel under a 100 V bias. The weighted center of intensity velocity was extracted as DNA molecules traversed the field of view and is plotted against four locations in the device (figure 3(a)). Three molecules were analyzed for each location. Deviations from the average velocity were greatest for data taken just before the 150 μm channel entrance, where the depth change across the field of view was greatest. Deviations inside the 150 μm channel are due to the shorter time each molecule occupied the field of view. Average velocities increased by a factor of 70, rather than the factor of 5 expected solely due to differences in the electric field strength arising from changing channel width without a depth gradient. Velocities were observed to increase smoothly, indicating continuous depth change.

λ DNA molecules were also driven electrokinetically into the h-junction devices shown in table 2. Figure 3(b) shows fluorescence micrographs of λ DNA molecules in a 3 mm wide loading channel of the shallowest device in table 2. The out-of-plane deflection was sufficient to accommodate DNA molecules in their bulk radius of gyration. Figure 3(c) shows two DNA molecules loaded into the 7 nm deep, 300 μm wide slit-like nanochannel and confined by the dense matrix of surface roughness features (surface roughness: 0.8 nm). DNA molecules often remained stretched around these features upon removal of the applied electric field, which may be useful for applications requiring DNA elongation and observation, such as single molecule genomic mapping [9].

Radius of gyration, R_g, measurements taken in the remaining devices in table 2 are plotted in figure 3(d) versus channel depth. Data were obtained for each nanochannel depth from ten λ DNA molecules far enough away from channel walls and entrances to minimize any resulting effects on the behavior of the molecules. The 507 nm deep, 150 μm wide nanochannel was fabricated identically to the other devices but without the use of nanoglassblowing. The widths of the other channels used were as follows: 100 μm (156 nm deep channel); 300 μm (70 nm deep channel); 100 μm (36 nm deep channel); and 300 μm (11 nm deep channel). The depth of field of the microscope objective used (60× 1.2 NA water immersion objective (Olympus)) was approximately 500 nm, ensuring that molecules were in focus for all channel depths. DNA molecules in the 507 nm deep nanochannel were imaged with an additional 1.5× magnification provided by internal microscope lenses. Raw video frames were processed using averaging and Gaussian digital filters and thresholded and

binarized using Otsu's method. Connected regions of eight pixels or greater were used to identify pixels comprising the molecule. The total variation of R_g across the reasonable ranges of parameters associated with filtering and thresholding was found to be approximately 9%. From these processed images, R_g was computed as the trace of the second moment of the intensity tensor of a DNA molecule [14, 15]:

$$M_{ij}(t) = \frac{1}{I(t)} \int (r_i - R_{cm,i})(r_j - R_{cm,j}) I(r,t)\,dr,$$

where t is time, $I(t)$ is the total intensity of the molecule, $I(r,t)$ is the intensity distribution of the molecule, R_{cm} is the intensity-weighted center of the molecule, r is the position of a pixel considered to be part of the molecule, and R_g is given by [14, 15]:

$$R_g = \sqrt{\mathrm{trace}(M_{ij})}$$

for each of approximately 100–400 consecutive frames taken at 10 frames s^{-1}. Numerical simulations were used to explore the effects of diffraction limited optical resolution and image pixelation on measurements of R_g. Simple model molecules were generated, convolved with a Gaussian approximation of the point spread function (with an Airy radius of 0.27 μm calculated from optical parameters and fluorescence emission wavelengths), and binned according to the camera pixel size of 16 μm by 16 μm. R_g values for these simulated images were larger than those of corresponding model molecules by approximately 4.2% to 0.9% for compact and elongated molecules, respectively. The weighted average of the mean R_g for each channel depth was then reduced by (2.6 ± 1.7)% to account for these effects. The error bars in figure 3(d) represent the sum of the error values associated with optical resolution, image pixelation, digital filtering, and noise thresholding. One standard deviation on the weighted average of the mean is also included in the error bars and is small compared to the other sources of uncertainty. The distributions of the radius of gyration measurements for single molecules were not used to compute the error, because these values reflect the physical motion of the DNA molecules in the channel in addition to any measurement or systematic errors.

Because the slit-like nanochannel depths potentially span multiple regimes of DNA confinement, the same theoretical model may not describe data from all channel depths. The R_g results presented for channel depths from 36 to 156 nm are in qualitative agreement with Brochard's prediction of $R_g \propto d^{-0.25}$, shown in figure 3(d) as a dashed line, for a polymer pancake composed of blobs [36] in a slit-like nanochannel [37]. Data from the 507 nm deep channel deviates from Brochard's prediction, perhaps because the molecules did not form enough blobs to follow the predicted power law. These data may also be subject to additional error due to the confinement of each molecule to a space approximately equal to the objective's depth of field. Data from the 11 nm deep channel deviate from the theoretical power law, possibly due to channel surface roughness, unobserved out-of-plane curvature in this nanochannel, or the onset of another regime of confinement dynamics. This last possibility is supported by the expected failure of the blob model as d decreases to the point where the polymer is influenced along its entire length by the confining dimension. The existing theoretical formulation for such a highly confined polymer composed of reflecting rods in slit-like nanochannels contains a dependence on channel width [7, 9, 25] and is consequently not applicable to DNA in the wide nanochannels used here. Recent measurements in roughly square nanochannels suggest that the cross-over between blob and reflecting rod behavior for DNA lies near a channel depth of 100 nm [25], while the measurements shown here suggest a transition at a much smaller channel depth for slit-like nanochannels. Further work examining highly confined DNA in slit-like nanochannels is needed to develop a clear theoretical understanding of DNA behavior in these nanoscale environments.

4. Conclusions

Nanoglassblowing is presented as a method for fabricating smoothly integrated microfluidic and nanofluidic devices. Fused silica devices with out-of-plane curvature of channel covers and wide, shallow nanochannels were constructed using this method and applied to the manipulation and analysis of single biomolecules. The utility of gradual changes in channel depth at the interface between deeper loading regions and planar, slit-like nanochannels was demonstrated. Nanochannel depths and aspect ratios formed by nanoglassblowing facilitated single molecule measurements of the radius of gyration of λ DNA molecules constrained to slit-like nanochannels with depths ranging from 11 nm to 507 nm, providing insight into the behavior of DNA in this type of confining nanoscale geometry. Nanoglassblowing has the potential to extend the availability and utility of glass microfluidic and nanofluidic devices by providing a simple means to fabricate and integrate non-planar device features, continuous changes in channel depth ranging from tens of micrometers to a few nanometers, and wide, shallow nanochannels.

Acknowledgments

The work was supported in part by the Nanobiotechnology Center (NBTC), an STC Program of the National Science Foundation under Agreement No. ECS-9876771. Device fabrication was performed at the Cornell Nanoscale Facility, a member of the National Nanotechnology Infrastructure Network, and the Cornell Center for Materials Research, both supported by the National Science Foundation. This research was performed while Dr Samuel Stavis held a National Research Council Research Associateship Award at the NIST. The authors would like to thank Dr Christian Reccius and Dr Stephen Levy for use of their Labview and Matlab programs and Mr Leon Bellan for assistance performing atomic force microscopy.

Certain commercial equipment and materials are identified in this paper to foster understanding. Such identification does not imply recommendation or endorsement by the National Institute of Standards and Technology, nor does it imply that the materials and equipment identified are necessarily the best available for the purpose.

References

[1] Stavis S M, Corgié S C, Cipriany B R, Craighead H G and Walker L P 2007 *Biomicrofluidics* **1** 034105
[2] Bakajin O B, Duke T A J, Chou C F, Chan S S, Austin R H and Cox E C 1998 *Phys. Rev. Lett.* **80** 2737–40
[3] Mannion J and Craighead H G 2007 *Biopolymers* **85** 131–43
[4] Tegenfeldt J O, Prinz C, Cao H, Huang R L, Austin R H, Chou S Y, Cox E C and Sturm J C 2004 *Anal. Bioanal. Chem.* **378** 1678–92
[5] Pennathur S, Baldessari F, Santiago J G, Kattah M G, Steinman J B and Utz P J 2007 *Anal. Chem.* **79** 8316–22
[6] Fu J, Schoch R B, Stevens A L, Tannenbaum S R and Han J 2007 *Nat. Nanotechnol.* **2** 121–8
[7] Odijk T 2006 *J. Chem. Phys.* **125** 204904
[8] Balducci A, Mao P, Han J and Doyle S P 2006 *Macromolecules* **39** 6273–81
[9] Jo K, Dhingra D M, Odijk T, de Pablo J J, Graham M D, Runnheim R and Schwartz D C 2007 *Proc. Natl Acad. Sci. USA* **104** 2673–8
[10] Krishnan H, Monch I and Schwille P 2007 *Nano Lett.* **7** 1270–5
[11] Chen Y-L, Graham M D and de Pablo J J 2004 *Phys. Rev.* E **70** 060901
[12] Cross J D, Strychalski E A and Craighead H C 2007 *J. Appl. Phys.* **102** 024701
[13] Thamdrup L H, Persson F, Bruus H, Kristensen A and Flyvberg H 2007 *Appl. Phys. Lett.* **91** 163505
[14] Lin P-K, Fu C-C, Chen Y-L, Chen Y-R, Wei P-K, Kuan C H and Fann W S 2007 *Phys. Rev.* E **76** 011806
[15] Maier B and Radler J O 2000 *Macromolecules* **33** 7185–94
[16] Hsieh C, Balducci A and Doyle P S 2006 *Macromolecules* **39** 6273–81
[17] Cao H, Tegenfeldt J O, Austin R H and Chou S Y 2002 *Appl. Phys. Lett.* **81** 3058–60
[18] Gu J, Gupta R, Chou C-F, Wei Q and Zenhausern F 2007 *Lab Chip* **7** 1198–201
[19] Eklund E J and Shkel A M 2007 *J. Microelectromech. Syst.* **16** 232–9
[20] Huff M A, Nikolich A D and Schmidt M A 1993 *J. Microelectromech. Syst.* **2** 74–81
[21] Turner S W P, Cabodi M and Craighead H G 2002 *Phys. Rev. Lett.* **88** 128103
[22] Han J, Turner S W and Craighead H G 1999 *Phys Rev. Lett.* **83** 1688–91
[23] Han J and Craighead H G 2000 *Science* **288** 1026–9
[24] Reccius C H, Stavis S M, Mannion J T, Walker L P and Craighead H G 2008 *Biophys. J.* doi:10.1529/biophysj.107.121020
[25] Reisner W, Beech J P, Larsen N B, Flyvbjerg H, Kristensen A and Tegenfeldt J O 2007 *Phys. Rev. Lett.* **99** 058302
[26] Huh D, Bahng J H, Ling Y, Wei H-H, Kripfgans O D, Fowlkes J B, Grotberg J B and Takayama S 2007 *Anal. Chem.* **79** 1369–76
[27] Sethnu P, Sin A and Toner M 2006 *Lab Chip* **6** 83–9
[28] Singh K, Su X, Liu C, Capjack C, Rozmus W and Backhouse C J 2006 *Cytometry* A **69A** 307–15
[29] Demetri P, Quake S R and Yang C 2006 *Nature* **442** 381–6
[30] Fidkowski C, Kaazempur-Mofrad M R, Borenstein J, Vacanti J P, Langer R and Wang Y 2005 *Tissue Eng.* **11** 302–9
[31] Lim D, Kamotani Y, Cho B, Mazumder J and Takayama S 2003 *Lab Chip* **3** 318–23
[32] Park S, Wolanin P M, Yuzbashyan E A, Lin H, Darnton N C, Stock J B, Silberzan P and Austin R 2003 *Proc. Natl Acad. Sci. USA* **100** 13910–5
[33] Newton Sir Issac 1952 *Opticks: or a Treatise of the Reflections, Refractions, Inflections and Colours of Light* 4th edn (New York: Dover) p 232
[34] Lin C and Sullivan R F 1972 *IBM J. Res. Dev.* **16** 269–76
[35] Mao P and Han J 2005 *Lab Chip* **5** 837–44
[36] de Gennes P-G 1979 *Scaling Concepts in Polymer Physics* (Ithaca, NY: Cornell University Press)
[37] Brochard F 1977 *J. Physique* **38** 1285–91